First-Principles Calculations on Attosecond Transient Absorption Spectroscopy for Bulk Nickel

Shunsuke A. Sato
Department of Physics, Tohoku University
Sendai 980-8578, Japan

1 Introduction

Light-driven electron dynamics in solids is a central subject in ultrafast condensed-matter physics. Intense and ultrashort optical fields can drive electrons far from equilibrium and modify the optical and magnetic properties of materials on femtosecond and attosecond time scales. Recent progress in attosecond spectroscopy has made it possible to probe such electronic motion directly in the time domain, including light-induced spin dynamics in magnetic materials through attosecond circular dichroism [1]. These developments require microscopic theories that connect the electron dynamics induced by a pump pulse to the transient optical response measured by an attosecond probe.

Attosecond transient absorption spectroscopy (ATAS) is a useful approach for investigating ultrafast electron dynamics in solids because it measures pump-induced changes in the absorption spectrum with attosecond temporal resolution. In magnetic transition metals, the absorption around the $M_{2,3}$ edge is especially informative, since it involves optical transitions from $3p$ semicore states to unoccupied states with substantial $3d$ character. The spectral response in this region is sensitive to the exchange splitting of the semicore states and to the microscopic screening associated with localized $3p$–$3d$ electronic response. Therefore, ATAS with linearly polarized probe pulses can provide a complementary route to magnetic dynamics, although the measured transient spectrum is not a direct magnetic observable.

The interpretation of ATAS spectra in solids is generally difficult because the macroscopic optical response reflects several microscopic processes at the same time. Previous first-principles studies of magnetic transition metals have shown that transient absorption spectra around the $M_{2,3}$ edge contain both magnetic and nonmagnetic electronic contributions [2, 3]. A reduction of the local spin polarization and of the associated exchange splitting of the $3p$ semicore states can produce a narrow absorption decrease near the edge. In contrast, pump-induced charge redistribution and the modification of microscopic screening and local-field effects can generate a broader absorption increase. Thus, even near a magnetic semicore edge, the transient absorption spectrum must be interpreted as a combined response of spin-dependent electronic structure and charge-screening dynamics. While this two-component picture has been examined in finite-electron-temperature calculations for magnetic materials and in explicit nonequilibrium pump–probe simulations for bulk Co, its applicability to laser-driven ferromagnetic Ni in a fully real-time nonequilibrium calculation remains to be clarified.

First-principles real-time time-dependent density functional theory (TDDFT) provides a direct way to address this problem [5]. By solving the time-dependent Kohn–Sham equation in the presence of pump and probe fields, one

can simulate the pump–probe process and evaluate the transient optical response from the induced current [4, 3]. This approach is useful for connecting microscopic electronic motion in a driven solid to experimentally relevant optical quantities such as the transient dielectric function and absorption coefficient. In addition, comparison with finite-electron-temperature calculations provides a reference for quasi-equilibrium hot-electron states and helps distinguish thermalized electronic effects from coherent nonequilibrium dynamics during and shortly after pump irradiation.

In this work, we study ATAS of bulk ferromagnetic Ni using first-principles real-time TDDFT. Ni is a prototypical itinerant ferromagnet with a relatively small magnetic moment and a clear $M_{2,3}$ absorption edge originating from $3p$ semicore states. It therefore provides a useful test case for examining how the magnetic sensitivity of the $M_{2,3}$ edge appears in a nonequilibrium optical response. We first analyze the equilibrium electronic structure and optical response of Ni, then introduce finite-electron-temperature calculations as quasi-equilibrium references, and finally perform explicit pump–probe simulations around the Ni $M_{2,3}$ edge. The aim of the present study is to clarify how the ultrafast electron dynamics of laser-driven ferromagnetic Ni are reflected in the transient absorption spectrum, and to examine to what extent the two-component interpretation established in earlier studies of magnetic transition metals applies to Ni in a real-time nonequilibrium calculation.

2 Methods

2.1 First-principles electron dynamics calculations

We investigate the transient optical response of bulk ferromagnetic Ni using real-time TDDFT for periodic solids. The first-principles electron dynamics method is summarized here; further details are given elsewhere [3, 6]. Unless otherwise stated, atomic units are used. The ions are fixed at their equilibrium positions, which is appropriate for the electronic time scale considered in this work.

In the collinear spin-polarized formulation, the electron dynamics is described by the time-dependent Kohn–Sham equation for the periodic part of the Bloch orbital,

$$i\frac{\partial}{\partial t}u_{bs\boldsymbol{k}}(\boldsymbol{r},t) = \hat{h}_{s\boldsymbol{k}}(t)u_{bs\boldsymbol{k}}(\boldsymbol{r},t), \tag{1}$$

where b is the band index, $s = \uparrow, \downarrow$ is the spin index, and $\boldsymbol{k}$ is the Bloch wave vector. The time-dependent Kohn–Sham Hamiltonian is

$$\begin{aligned}\hat{h}_{s\boldsymbol{k}}(t) &= \frac{1}{2}\left[\boldsymbol{p}+\boldsymbol{k}+\boldsymbol{A}(t)\right]^2 \\ &+ \hat{v}_{\mathrm{ion}} + v_{\mathrm{Hxc},s}[\rho_\uparrow(\boldsymbol{r},t),\rho_\downarrow(\boldsymbol{r},t)]\end{aligned} \tag{2}$$

where $\hat{v}_{\mathrm{ion}}$ is the ionic pseudopotential and $v_{\mathrm{Hxc},s}$ is the spin-dependent Hartree–exchange–correlation potential. Here, $\rho_\uparrow(\boldsymbol{r},t)$ and $\rho_\downarrow(\boldsymbol{r},t)$ are the electron densities for the respective spin channels. The Hartree–exchange–correlation potential is evaluated within the adiabatic approximation, and exchange–correlation contributions to the vector potential are neglected. The applied electromagnetic field is treated in the long-wavelength approximation by a spatially uniform vector potential $\boldsymbol{A}(t)$, and the corresponding electric field is $\boldsymbol{E}(t) = -d\boldsymbol{A}(t)/dt$. Because the present study focuses on the Ni $M_{2,3}$ edge, the Ni $3p$ semicore states are explicitly included in the valence space of the pseudopotential calculation.

The initial orbitals are obtained from the self-consistent spin-polarized Kohn–Sham equation for ferromagnetic Ni. The occupation factors are given by the Fermi–Dirac distribution, $f_{bs\boldsymbol{k}} = \left[\exp\left[(\epsilon_{bs\boldsymbol{k}}-\mu)/(k_{\mathrm{B}}T_e)\right]+1\right]^{-1}$, where $\epsilon_{bs\boldsymbol{k}}$ is the Kohn–Sham eigenvalue, μ is the chemical potential, and T_e is the electron temperature. For the equilibrium and explicit pump–probe calculations, $T_e = 300$ K is used unless otherwise stated. The chemical potential is determined from charge neutrality, and

the occupation factors are kept fixed during the real-time propagation.

Spin–orbit coupling is not included. The spin quantization axis is therefore chosen as the z axis, and the time propagation remains diagonal in the spin index. Consequently, the number of electrons in each spin channel is conserved in the explicit pump–probe dynamics. The magnetic changes discussed below should therefore be understood as changes in the local spin polarization and in the associated spin-dependent electronic structure, rather than as spin-flip demagnetization. The notation $M_{2,3}$ denotes the Ni $3p$ semicore absorption region, without resolving the spin–orbit splitting between the M_2 and M_3 edges.

The macroscopic current density is evaluated as

$$\boldsymbol{J}(t) = -\frac{1}{\Omega_{\mathrm{cell}}} \sum_{b,s} \frac{1}{\Omega_{\mathrm{BZ}}} \int_{\mathrm{BZ}} d\boldsymbol{k}\, f_{bs\boldsymbol{k}} \times \int_{\mathrm{cell}} d\boldsymbol{r}\, u^*_{bs\boldsymbol{k}}(\boldsymbol{r},t) \hat{\boldsymbol{v}}_{s\boldsymbol{k}}(t) u_{bs\boldsymbol{k}}(\boldsymbol{r},t), \quad (3)$$

where Ω_{cell} and Ω_{BZ} are the volumes of the unit cell and Brillouin zone, respectively. The velocity operator is $\hat{\boldsymbol{v}}_{s\boldsymbol{k}}(t) = \left[\boldsymbol{r}, \hat{h}_{s\boldsymbol{k}}(t)\right]/i$.

2.2 Computational details

All calculations are performed with the Octopus code in a real-space, real-time framework [7]. Bulk Ni is modeled by the fcc crystal structure with lattice constant $a = 3.52$ Å. The fcc unit cell is discretized into 28^3 real-space grid points, and the Brillouin zone is sampled with 24^3 k-points. Norm-conserving pseudopotentials are employed, and the Ni $3s$, $3p$, $3d$, and $4s$ electrons are treated explicitly as valence electrons. The exchange–correlation functional is the adiabatic local spin-density approximation [8].

3 Results

3.1 Electronic structure and equilibrium optical response

We first examine the equilibrium electronic structure and optical response of bulk Ni, which serve as references for the transient spectra discussed below. Figure 1 shows the spin-resolved band structure in a wide energy window, with the Fermi level set to zero. The bands near the Fermi level show the metallic character expected for elemental Ni. In addition, nearly dispersionless semicore bands appear around 60 eV below the Fermi level and are assigned to the Ni $3p$ states. Both the valence and semicore states are spin split in the ferromagnetic ground state. The exchange splitting of the Ni $3p$ semicore bands is about 1 eV, which provides an important microscopic energy scale for the $M_{2,3}$-edge response.

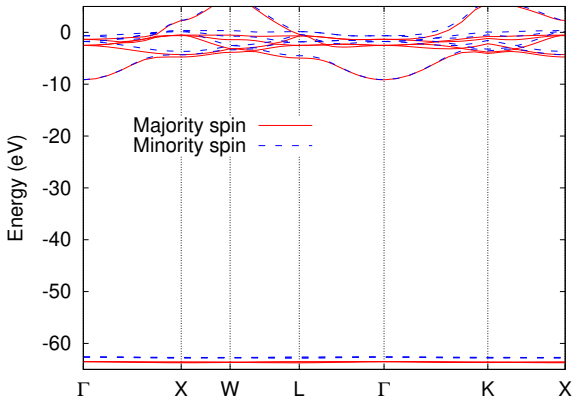

Figure 1: Spin-resolved band structure of ferromagnetic bulk Ni in a wide energy window. The Fermi level is set to 0 eV. Majority- and minority-spin bands are shown separately.

The $M_{2,3}$-edge absorption considered here mainly originates from optical transitions from the $3p$ semicore states to unoccupied states with substantial $3d$ character near the Fermi level. The spectrum is therefore sensitive not only to the spin-dependent positions of the semicore levels but also to the microscopic

screening associated with the localized $3p$–$3d$ electronic response. This point is important for interpreting the transient spectra, because the edge region contains magnetic information through the exchange splitting of the semicore states and nonmagnetic electronic information through charge redistribution and local-field effects.

The equilibrium optical response is obtained from a real-time linear-response calculation. A weak impulsive distortion is applied along a Cartesian direction β through

$$\boldsymbol{A}_{\mathrm{imp}}^{(\beta)}(t) = -k_0 \boldsymbol{e}_\beta \Theta(t), \tag{4}$$

where k_0 is sufficiently small to remain in the linear-response regime, $\boldsymbol{e}_\beta$ is a unit vector along the β direction, and $\Theta(t)$ is the Heaviside step function. From the induced current, the optical conductivity tensor is evaluated as

$$\sigma_{\alpha\beta}(\omega) = \frac{1}{k_0} \int_0^\infty dt\, J_\alpha^{(\beta)}(t) e^{i\omega t - \gamma t}, \tag{5}$$

where γ is a damping parameter introduced to suppress finite-time artifacts. We use $\gamma = 0.5$ eV in the Fourier analysis. The dielectric tensor and absorption coefficient are then obtained as

$$\varepsilon_{\alpha\beta}(\omega) = \delta_{\alpha\beta} + \frac{4\pi i}{\omega} \sigma_{\alpha\beta}(\omega), \tag{6}$$

and

$$\mu_\alpha(\omega) = \frac{2\omega}{c} \mathrm{Im}\left[\sqrt{\varepsilon_{\alpha\alpha}(\omega)}\right]. \tag{7}$$

The equilibrium absorption spectrum in the Ni $M_{2,3}$-edge region is used as the reference for the transient absorption spectra.

Figure 2 (a) shows the current induced by the weak impulsive distortion at $t = 0$. The current is generated immediately after the perturbation and subsequently exhibits dephasing among electronic transitions. In the Fourier analysis, the exponential damping factor further suppresses finite-time artifacts. The dielectric function is obtained from this current according to the procedure described above.

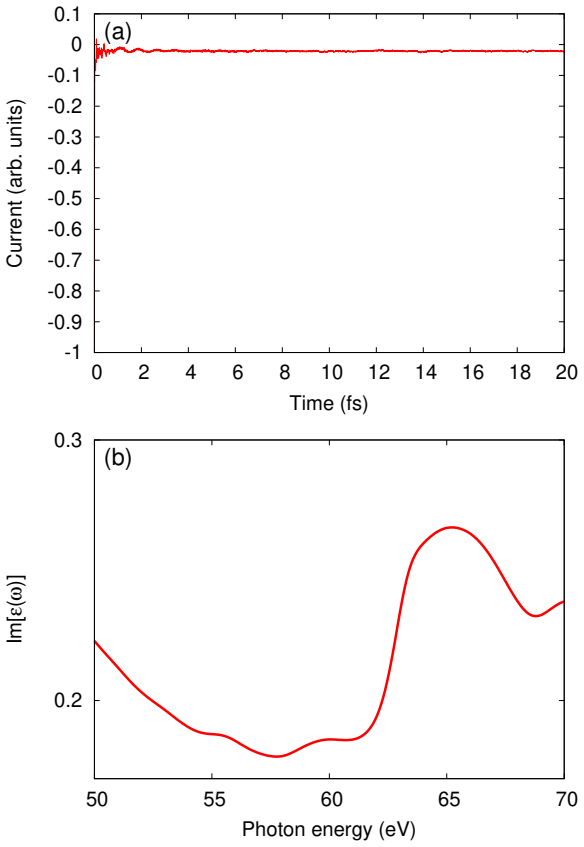

Figure 2: Equilibrium linear response of bulk Ni. (a) Current induced by a weak impulsive perturbation. (b) Imaginary part of the dielectric function around the Ni $M_{2,3}$ edge.

Figure 2 (b) shows the imaginary part of the dielectric function around the Ni $M_{2,3}$ edge. The calculated spectrum exhibits a sharp increase in the absorption-related response near the edge. Because the spectral weight changes rapidly in this energy region, a small pump-induced modification of the edge position or line shape can produce a localized structure in the differential spectrum. The spin splitting of the Ni $3p$ states is therefore expected to affect the transient signal through the edge position. In particular, a reduction of the local exchange splitting can shift the edge-related spectral weight and lead to a narrow absorption decrease in the differential response, as discussed below.

3.2 Finite-electron-temperature reference for the Ni $M_{2,3}$ edge

Before analyzing the explicit pump–probe response, we introduce a finite-T_e linear-response calculation as a quasi-equilibrium reference for a hot-electron state of Ni [9]. This reference is useful for separating spectral changes that can be attributed to electronic redistribution and the self-consistent modification of the electronic structure from those specific to the coherent nonequilibrium dynamics generated by the pump pulse. For a given electron temperature T_e, the occupation factors are replaced by the corresponding Fermi–Dirac distribution, and the static Kohn–Sham potential is recomputed self-consistently under the charge-neutrality condition. The optical response is then evaluated by the same impulsive-distortion procedure as in the equilibrium calculation. Thus, the finite-T_e calculation does not simulate the pump–probe dynamics itself, but provides the optical response of a quasi-equilibrium electronic state with a cold lattice.

The finite-T_e changes in the dielectric function and absorption coefficient are defined relative to the 300 K ferromagnetic state as

$$\Delta\varepsilon_{\alpha\alpha}(\omega;T_e) = \varepsilon_{\alpha\alpha}(\omega;T_e) - \varepsilon_{\alpha\alpha}(\omega;300\ \mathrm{K}), \quad (8)$$

and

$$\Delta\mu_{\alpha}(\omega;T_e) = \mu_{\alpha}(\omega;T_e) - \mu_{\alpha}(\omega;300\ \mathrm{K}). \quad (9)$$

The finite-T_e response includes the effect of state filling through the Fermi–Dirac occupations, the self-consistent change in the spin-dependent Kohn–Sham potential, and the modification of microscopic screening and local-field effects through the time-dependent Hartree–exchange–correlation potential.

Figure 3 shows the change in $\mathrm{Im}[\varepsilon(\omega)]$ for several electron temperatures, measured relative to the 300 K ferromagnetic state. The labels in the figure denote the electron temperature in energy units. The calculated response is not a uniform increase or decrease of the equilibrium spectrum. Instead, positive and negative components appear in the photon-energy region of the Ni $M_{2,3}$ edge, showing that the finite-T_e modification changes both the spectral weight and the line shape near the edge.

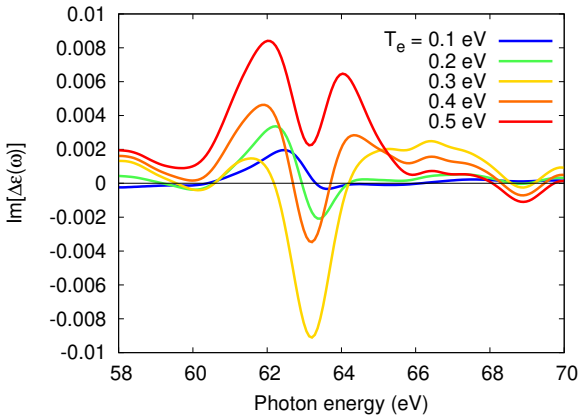

Figure 3: Change in the imaginary part of the dielectric function of Ni obtained from finite-electron-temperature reference calculations. The change is measured relative to the 300 K ferromagnetic state.

The spectral features in Fig. 3 can be understood as the combination of two main contributions [2]. One is a relatively narrow edge-related change associated with the reduction of the local spin polarization and the corresponding exchange splitting of the Ni $3p$ semicore states. The other extends over a broader photon-energy range and is associated with changes in charge redistribution, state filling, and microscopic screening. The localized character and large spatial overlap of the $3p$ and $3d$ states make the response particularly sensitive to local-field effects, as already indicated by the equilibrium optical response.

The finite-electron-temperature analysis therefore provides a useful quasi-equilibrium reference for the electronic state after thermalization. However, it cannot describe coherent subcycle modulations during pump–probe overlap, nor does it represent the nonthermal occupation pattern produced immediately

by the pump pulse. To analyze the optical response in the nonequilibrium phase more directly, we next perform real-time pump–probe TDDFT simulations.

3.3 Attosecond transient absorption

We next evaluate the transient optical response by explicit pump–probe TDDFT simulations [4]. The electron dynamics are calculated in the presence of the pump and probe vector potentials,

$$\boldsymbol{A}(t;\tau) = \boldsymbol{A}_{\mathrm{pump}}(t) + \boldsymbol{A}_{\mathrm{probe}}(t-\tau), \quad (10)$$

where τ is the delay between the centers of the pump and probe pulses. The pump pulse drives the electronic system of Ni out of equilibrium, whereas the probe pulse is kept sufficiently weak so that the probe-induced response can be treated as linear on top of the pump-driven state.

In the present study, the pump pulse is given by

$$\boldsymbol{A}_{\mathrm{pump}}(t) = -\frac{E_{\mathrm{pump}}}{\omega_{\mathrm{pump}}}\boldsymbol{e}_{\mathrm{pump}} \times \cos^2\left(\frac{\pi t}{T_{\mathrm{pump}}}\right)\sin(\omega_{\mathrm{pump}}t) \quad (11)$$

for $|t| < \frac{T_{\mathrm{pump}}}{2}$, and is zero otherwise. The probe pulse is given by

$$\boldsymbol{A}_{\mathrm{probe}}(t-\tau) = -\frac{E_{\mathrm{probe}}}{\omega_{\mathrm{probe}}}\boldsymbol{e}_{\mathrm{probe}} \times \cos^4\left[\frac{\pi(t-\tau)}{T_{\mathrm{probe}}}\right]\sin\left[\omega_{\mathrm{probe}}(t-\tau)\right] \quad (12)$$

for $|t-\tau| < \frac{T_{\mathrm{probe}}}{2}$, and is zero otherwise. The pump parameters are $\hbar\omega_{\mathrm{pump}} = 1.55$ eV, $T_{\mathrm{pump}} = 20$ fs, $E_{\mathrm{pump}} = 2.7$ MV/cm. The pump and probe polarizations are taken to be parallel. The probe duration is $T_{\mathrm{probe}} = 1$ fs, and the central photon energy is chosen so that the probe spectrum covers the Ni $M_{2,3}$-edge region. The probe field strength is sufficiently small compared with the pump field.

For each delay τ, two real-time calculations are performed. The pump-only calculation gives the current $\boldsymbol{J}_{\mathrm{pump}}(t)$, whereas the pump–probe calculation gives the current $\boldsymbol{J}_{\mathrm{pump+probe}}(t;\tau)$. The current induced by the probe pulse in the pump-driven state is then extracted as

$$\Delta\boldsymbol{J}_{\mathrm{probe}}(t;\tau) = \boldsymbol{J}_{\mathrm{pump+probe}}(t;\tau) - \boldsymbol{J}_{\mathrm{pump}}(t). \quad (13)$$

This subtraction removes the nonlinear current generated solely by the pump pulse and isolates the response to the weak probe field. The transient optical conductivity is obtained by comparing the Fourier component of this probe-induced current with that of the probe electric field,

$$\sigma^{\mathrm{tr}}_{\alpha\beta}(\omega,\tau) = \frac{\int dt\, \Delta J_{\mathrm{probe},\alpha}(t;\tau)e^{i\omega t-\gamma t}}{\int dt\, E_{\mathrm{probe},\beta}(t-\tau)e^{i\omega t-\gamma t}}. \quad (14)$$

The same damping parameter as in the equilibrium linear-response calculation is used in the Fourier analysis. The transient dielectric tensor and absorption coefficient are then evaluated as

$$\varepsilon^{\mathrm{tr}}_{\alpha\beta}(\omega,\tau) = \delta_{\alpha\beta} + \frac{4\pi i}{\omega}\sigma^{\mathrm{tr}}_{\alpha\beta}(\omega,\tau), \quad (15)$$

and

$$\mu^{\mathrm{tr}}_{\alpha}(\omega,\tau) = \frac{2\omega}{c}\mathrm{Im}\left[\sqrt{\varepsilon^{\mathrm{tr}}_{\alpha\alpha}(\omega,\tau)}\right]. \quad (16)$$

The theoretical ATAS signal is defined as the differential absorption relative to the equilibrium response, $\Delta\mu_\alpha(\omega,\tau) = \mu^{\mathrm{tr}}_\alpha(\omega,\tau) - \mu_\alpha(\omega)$.

Figure 4 (a) shows the calculated differential absorption $\Delta\mu(\omega,\tau)$ around the Ni $M_{2,3}$ edge, and Fig. 4 (b) shows the pump electric field. During the temporal overlap of the pump and probe pulses, the spectrum exhibits rapidly varying structures. These structures reflect the coherent electron dynamics driven by the pump field and are therefore distinct from the quasi-equilibrium response discussed in the finite-T_{e} calculation.

After the main part of the pump pulse has passed, the spectrum becomes simpler and more persistent. The post-pump response is not described by a rigid shift or by a uniform

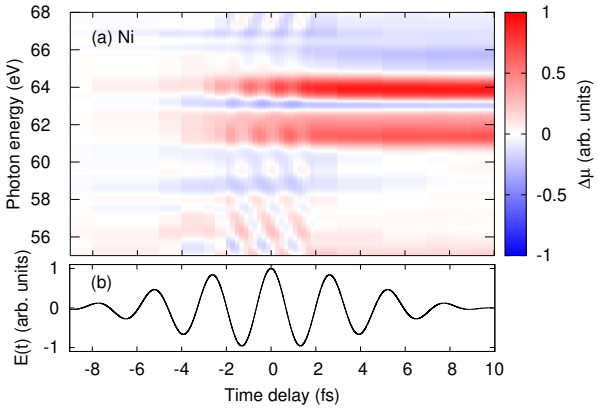

Figure 4: Attosecond transient absorption of bulk Ni from the real-time pump–probe TDDFT simulation. (a) Differential absorption $\Delta\mu(\omega, \tau)$ around the Ni $M_{2,3}$ edge. (b) Pump electric field as a function of delay.

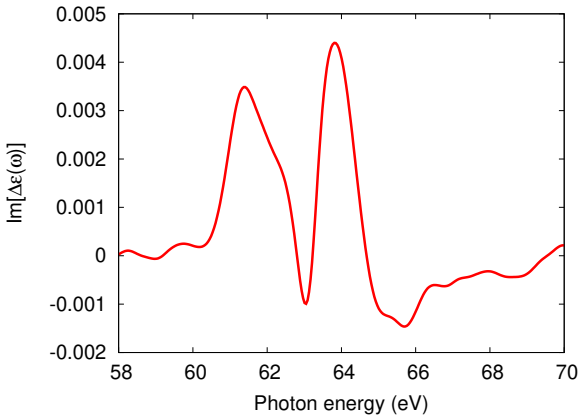

Figure 5: Change in the imaginary part of the dielectric function due to the pump field at the delay of 10 fs. The change is evaluated relative to the equilibrium response.

amplitude change of the equilibrium spectrum. Instead, it contains positive spectral weight over a relatively broad photon-energy range, together with a narrower negative component near the steep edge structure around the Ni $M_{2,3}$ edge. This form already indicates that the transient absorption contains more than one microscopic contribution.

To compare the pump–probe result with the finite-electron-temperature reference more directly, Fig. 5 shows the change in the imaginary part of the dielectric function at the delay of 10 fs. The spectrum contains positive peaks in the lower part of the edge region and negative components near and above the edge. This line shape is qualitatively consistent with the two-component structure found in the finite-electron-temperature calculation in Fig. 3. The detailed profile is different, however, because the explicit pump–probe calculation describes a coherent nonthermal electronic state, not a self-consistent hot-electron distribution.

The narrow negative component around the edge can be interpreted as a consequence of a pump-induced reduction of the local exchange splitting of the Ni $3p$ semicore states. Because the $M_{2,3}$-edge absorption involves transitions from the $3p$ semicore states to unoccupied states with substantial $3d$ character, a change in the $3p$ exchange splitting modifies the effective edge position. This produces an edge-localized decrease in the differential spectrum, similar to the behavior discussed in the finite-electron-temperature reference calculation [2]. Since spin–orbit coupling is not included here, the total number of electrons in each spin channel is conserved during the propagation. Therefore, this effect should not be described as spin-flip demagnetization. Within the present approximation, it reflects changes in the local spin polarization and in the associated spin-dependent electronic structure.

The broader positive contribution has a different origin. Following the interpretation established for transition-metal $M_{2,3}$-edge transient absorption [2, 3], this component is naturally associated with pump-induced changes in microscopic screening and local-field effects. It is linked to the redistribution of electronic charge around the Ni atoms and is not specific to ferromagnetic order. Thus, the Ni $M_{2,3}$-edge ATAS signal should not be interpreted as a direct measure of the magnetization alone. Even near a magnetic semicore

edge, the macroscopic optical response contains both magnetic information and nonmagnetic charge-screening dynamics.

4 Summary

We have investigated attosecond transient absorption spectroscopy of bulk ferromagnetic Ni using first-principles real-time TDDFT. The calculation explicitly treats the Ni $3p$ semicore states and evaluates the transient optical response around the $M_{2,3}$ edge. The purpose of the study was to clarify how the microscopic electron dynamics induced by an ultrashort pump pulse are reflected in the macroscopic absorption spectrum of a magnetic transition metal.

The finite-electron-temperature calculations provided a quasi-equilibrium reference and showed that the change in $\mathrm{Im}[\varepsilon(\omega)]$ near the $M_{2,3}$ edge is not a simple uniform increase or decrease of the equilibrium spectrum. Instead, positive and negative spectral components appear in the edge region, indicating that the transient response contains contributions from both spin-dependent electronic-structure changes and charge-screening dynamics.

The explicit pump–probe TDDFT simulations showed that the calculated differential absorption $\Delta\mu(\omega, \tau)$ exhibits rapidly varying structures during the temporal overlap of the pump and probe pulses, reflecting coherent nonequilibrium electron dynamics. After the main part of the pump pulse has passed, the response becomes more persistent and contains a broad positive contribution together with a narrower negative component near the $M_{2,3}$ edge. The line shape of the corresponding change in $\mathrm{Im}[\varepsilon(\omega)]$ is qualitatively consistent with the two-component structure found in the finite-T_e reference calculation.

The narrow edge-related negative component is attributed to a reduction of the local spin polarization and of the associated exchange splitting of the Ni $3p$ semicore states. In contrast, the broader positive contribution is associated with pump-induced charge redistribution and the modification of microscopic screening and local-field effects. Because spin–orbit coupling is not included in the present calculation, the magnetic change discussed here should be understood as a change in local spin polarization and spin-dependent electronic structure, rather than spin-flip demagnetization. These results show that the Ni $M_{2,3}$-edge ATAS signal encodes both magnetic and nonmagnetic electronic dynamics, and that a direct real-time TDDFT pump–probe simulation provides a useful microscopic basis for interpreting the macroscopic transient optical response of laser-driven ferromagnetic Ni.

References

[1] F. Siegrist *et* al.: Nature **571**, 240 (2019).

[2] S. A. Sato: Electron. Struct. **4**, 014007 (2022).

[3] S. A. Sato, H. Hübener, U. De Giovannini, A. Rubio: npj Computational Materials **11**, 233 (2025).

[4] S. A. Sato, K. Yabana, Y. Shinohara, T. Otobe, G. F. Bertsch Phys. Rev. B **89**, 064304 (2014).

[5] E. Runge, E. K. U. Gross: Phys. Rev. Lett. **52**, 997 (1984).

[6] S. A. Sato: Comput. Mater. Sci. **194**, 110274 (2021).

[7] N. Tancogne-Dejean *et* al.: J. Chem. Phys. **152**, 124119 (2020).

[8] J. P. Perdew, Y. Wang: Phys. Rev. B **45**, 13244 (1992).

[9] S. A. Sato, Y. Shinohara, T. Otobe, K. Yabana: Phys. Rev. B **90**, 174303 (2014).